Conformational states of the cytoprotective protein Bcl-xL

[1]Pavel Ryzhov, [1]Ye Tian, [1]Yong Yao, [1]Andrey A. Bobkov, [2]Wonpil Im and [1]Francesca M. Marassi*

[1] Sanford Burnham Prebys Medical Discovery Institute, 10901 North Torrey Pines Road, La Jolla CA, 92037.

[2] Departments of Biological Sciences, Chemistry, and Bioengineering, Lehigh University, PA 18015, USA

***Correspondence:** Francesca M. Marassi
Cancer Center
Sanford Burnham Prebys Medical Discovery Institute
10901 North Torrey Pines Road, La Jolla CA, 92037, USA
email: fmarassi@sbp.edu
phone: 858-795-5282

SIGNIFICANCE

The human protein Bcl-xL is a key regulator of programmed cell death in health and disease. Structural studies, important for understating the molecular basis for its functions, have advanced primarily by deleting both the long disordered loop that regulates its activity and the C-terminal tail that anchors the protein to intracellular membranes. Here we describe the preparation and conformations of full-length Bcl-xL in both its water-soluble and membrane-anchored states. The study provides new biophysical insights about Bcl-xL and its greater Bcl-2 protein family.

ABSTRACT

Bcl-xL is a major inhibitor of apoptosis, a fundamental homeostatic process of programmed cell death that is highly conserved across evolution. Because it plays prominent roles in cancer, Bcl-xL is a major target for anti-cancer therapy and for studies aimed at understanding its structure and activity. While Bcl-xL is active primarily at intracellular membranes, most studies have focused on soluble forms of the protein lacking both the membrane-anchoring C-terminal tail and the intrinsically disordered loop, which has resulted in a fragmented view of the protein's biological activity. Here we describe the conformation of full-length Bcl-xL. Using nuclear magnetic resonance (NMR) spectroscopy, molecular dynamics (MD) simulations, and isothermal titration calorimetry (ITC), we show how the three structural elements affect the protein's structure, dynamics and ligand binding activity in both its soluble and membrane-anchored states. The combined data provide information about the molecular basis for the protein's functionality and a view of its complex molecular mechanisms.

INTRODUCTION

Bcl-xL, a key suppressor of cell death in cancer, is a member of the Bcl-2 family of apoptosis regulatory proteins (1) and represents an important target for structural studies aimed at understanding its functional mechanisms (2, 3). Bcl-xL localizes predominantly to the mitochondrial outer membrane (4-7) but it also appears to exist in dynamic equilibrium between cytosolic and membrane-associated populations (8, 9). Its cytoprotective activity is associated with its ability to bind cytotoxic Bcl-2 proteins, thereby preventing their association with mitochondria and blocking mitochondrial membrane permeabilization and destabilization (10).

The first structures of Bcl-xL (11, 12) provided the framework for understanding how the Bcl-2 family proteins regulate apoptosis. Bcl-xL shares sequence and structural similarity with other Bcl-2 family members. Eight amphipathic α-helices, spanning four Bcl-2 homology (BH) motifs, fold to form a soluble globular head domain in which a surface-exposed hydrophobic groove serves as the primary binding site for the BH3 motifs of pro-apoptotic Bcl-2 ligands. A C-terminal tail is required for both membrane association and cytoprotective activity (9). Moreover, an intrinsically disordered loop located between helices α1 and α2 carries multiple sites for post-translational modifications – phosphorylation, deamidation and cleavage by caspases – that can dial the protein activity from cytoprotective to cytotoxic (13-34).

Structural studies have focused primarily on truncated forms of Bcl-xL lacking the C-terminal tail and/or the disordered loop (11, 12), which provides an incomplete view of the protein. Previously, we showed that the tail forms a transmembrane α-helix that anchors Bcl-xL to the lipid bilayer membrane while maintaining both the canonical structure of the globular head domain and its high-affinity for BH3 ligands (35, 36). The same conformation was observed for a construct where the C-terminal tail was connected to the head via a flexible sortase-A linker (37). Nevertheless, the roles of the disordered loop and tail have not been explored in the context of native, intact Bcl-xL, and precisely how the three protein components – head, tail and loop – work together to coordinate biological function in the cytosolic and membrane-anchored states remains incompletely understood. Here we combine data from nuclear magnetic resonance (NMR) spectroscopy, molecular dynamics (MD) simulation, and isothermal titration calorimetry (ITC) to describe how the three structural elements affect the structure and activity of soluble and membrane-anchored Bcl-xL.

MATERIALS AND METHODS

Protein Preparation and nanodisc preparation. The Bid_{BH3} peptide, corresponding to residues 80-99 in the BH3 domain of human Bid, was obtained commercially (GenScript) and dissolved directly in aqueous buffer. The MSP1D1Δh5 protein used for nanodisc preparation was produced in *E. coli* as described (38). Four sequences of Bcl-xL were prepared (Fig. S1A, B). Bcl-xL-ΔLΔC (residues 1-43, 85-212) was expressed and purified as described previously (35, 36). Bcl-xL-ΔL (residues 1-43, 85-233), Bcl-xL-ΔC (residues 1-212), and full-length Bcl-xL (residues 1-233) were expressed and purified with an intein expression system (39) as follows.

The DNA sequences were cloned into the NdeI and SapI restriction sites of the pTYB1 vector (New England Biolabs). This resulted in the C-terminus of Bcl-xL becoming fused to the N-terminus of the intein from *Saccharomyces cerevisiae* VMA1, followed by a chitin-binding domain from *Bacillus circulans*, which serves as affinity tag. Plasmids were transformed in *E. coli* BL21(DE3) cells, and cells were grown in M9 minimal media containing $(^{15}NH_4)_2SO_4$ and ^{13}C-glucose (Cambridge Isotope Laboratories) to obtain $^{15}N/^{13}C$ labeled protein. Cells were grown to OD_{600}=0.8, at 37°C, then induced with 1 mM isopropyl 1-thio-β-D-galactopyranoside and incubated with shaking at 18°C overnight. After harvesting by centrifugation (7,200 x g, 4 °C, 15 min) the cells were stored overnight at -80 °C. Cells harvested from 1 l of culture were suspended in 30 ml of buffer A (25 mM Tris-Cl pH 8, 150 mM NaCl, 1 mM EDTA) and lysed by three passes through a French press. The soluble extract was applied to 10 ml of chitin beads (New England Biolabs) equilibrated with chilled buffer A, and bound protein was washed extensively with buffer A. Cleavage of the intein from Bcl-xL was obtained by adding 20 ml of

30 mM dithiothreitol (DTT) in buffer A, and incubating the beads overnight, at 4°C, with gentle rocking. Cleaved Bcl-xL was eluted from the beads with buffer A and analyzed by SDS-PAGE.

For Bcl-xL-ΔC, the eluted fraction was concentrated and further purified by size exclusion chromatography (HiLoad 16/60 Superdex 75 column; GE Healthcare) in NMR buffer (25 mM Na-phosphate pH 6.5, 1 mM EDTA, 2 mM DTT). Protein fractions were verified by SDS PAGE and then transferred into NMR buffer by centrifugal concentration (Amicon Ultra 15 concentrator with 10 kD cutoff; Millipore) and stored at 4°C.

In the case of full-length Bcl-xL, the chitin elution fraction contained a substantial amount (~90%) of insoluble protein, which had to be removed by centrifugation (20,000 x g, 4°C, 30 min) before further purification. The soluble fraction was purified as described for Bcl-xL-ΔC. The insoluble fraction was dissolved in buffer B (25 mM Tris-Cl pH 8, 150 mM NaCl, 1 mM EDTA, 2 mM DTT, 6 M urea, 10 mM SDS) and then purified using size exclusion chromatography (HiLoad 16/600 Superdex 200; GE Healthcare) in buffer B. Purified protein was verified by SDS PAGE, then precipitated by dialysis against water, lyophilized and stored at -20°C.

Bcl-xL and Bcl-xL-ΔL were reconstituted in nanodiscs, starting from either soluble or insoluble purified protein, as described (35, 36). The nanodiscs contained 2 mg of Bcl-xL and had a protein to lipid molar ratio of 1:100. The membrane was composed of a 4:1 molar mixture of dimyristoyl-phosphatidylcholine (DMPC) and dimyristoyl-phosphatidylglycreol (DMPG). Bcl-xL nanodiscs were transferred to NMR buffer using an Amicon centrifugal concentrator.

***NMR experiments*.** Solution NMR experiments were performed on a Bruker Avance 600 MHz spectrometer with a $^{1}H/^{15}N/^{13}C$ triple-resonance Bruker cryoprobe. Chemical shifts were referenced to water (40). The ^{15}N, ^{1}HN, ^{13}CA and ^{13}CB resonances in the spectra of Bcl-xL-ΔC were assigned using $^{1}H/^{15}N/^{13}C$ triple-resonance HNCA (41) and HNCACB (42) experiments, and were deposited in the BMRB database (BMRB ID 50276). *Ab initio* resonance assignments for soluble and nanodisc-associated full-length Bcl-xL were precluded by low solubility and low sensitivity. The ^{15}N and ^{1}HN resonances of the soluble and nanodisc-associated states of native full-length Bcl-xL were assigned by direct comparison with the chemical shifts of Bcl-xL-ΔC assigned in this study, and of Bcl-xL-ΔLΔ(219-233) assigned previously (BMRB ID 25466) (35). Secondary structure was characterized by analyzing the chemical shifts with TALOS+ (43, 44). Combined chemical shift perturbations of ^{1}H and ^{15}N signals (ΔHN) were calculated as: $\Delta HN = [(\Delta H)^2+(\Delta N/5)^2]^{1/2}$. The NMR data were processed using TopSpin (Bruker) and analyzed using CCPNMR (45).

MD simulations. All-atom MD simulations were performed using the CHARMM36 force fields for protein and lipids (46-48), with the TIP3P water model (49), as described (50). Briefly, all systems were prepared using CHARMM-GUI *Solution Builder* and *Membrane Builder* (51-54), and equilibrated with the CHARMM-GUI standard protocol. The temperature and pressure were maintained at 303.15 K and 1 bar. MD production simulations were conducted with OpenMM (55) for 1 μs, and the last 500 ns of trajectories were used for analysis.

The initial structural models were generated as follows (Fig. S2). For soluble Bcl-xL, the head domain was taken from the structure (PDB 1BXL) of the Bcl-xL/Bak-BH3 complex which has both tail (residues 210-233) and loop (residues 45-84) deleted (12). The loop (residues 21-86) was taken from the structure (PDB 1LXL) of tail-truncated Bcl-xL (11). The helical tail (residues 210-233) was taken from the NMR structure (PDB: 6X7I) of the membrane-embedded C-terminal tail (36, 37) and docked in the BH3 groove by sequence-based alignment with the coordinates of the Bak-BH3 helix in the complex. The resulting model was solvated in water with 50 mM NaCl. The systems for MD simulation contained 29,324 water molecules and a total of 91,620 atoms, in a 100 Å x 100 Å x 100 Å box.

For membrane-anchored Bcl-xL, the head domain was taken from the structure (PDB 1LXL) of tail-truncated Bcl-xL (11), and the helical tail (residues 210-233) was taken from the NMR structure (PDB: 6X7I) (36) and then embedded in a phospholipid bilayer composed of a 4:1 molar ratio of DMPC and DMPG, surrounded by water with 50 mM NaCl. The systems for MD simulation contained 156 DMPC, 39 DMPG, and 16,802 water molecules and a total of 76,804 atoms, in a 100 Å x 100 Å x 150 Å box.

Five MD simulations were performed for each of the soluble and membrane-anchored states of Bcl-xL. For soluble Bcl-xL, the starting model was equilibrated for 100 ns and then used to seed five separate trajectories. For membrane-anchored Bcl-xL, five initial replicas were generated by moving the protein, embedded in the membrane with CHARMM-GUI, out of the membrane by 1Å, 2Å, 3Å and 4 Å along the z axis. These starting models also had different initial positions of the lipid molecules. This setup ensures that each MD run represents a distinct independent experiment.

The orientation of each helix relative to the membrane normal was obtained by calculating the geometry center (g) for the backbone heavy atoms of each overlapping set of four consecutive residues (residues i – i+3, i+1 – i+4, i+2 – i+5, ...) along each helix, and then fitting them to a single vector by linear regression. For each n-residue helix there are g=n-3 overlapping geometry centers.

***Isothermal Titration Calorimetry*.** Isothermal titration calorimetry experiments were performed using a Microcal iTC200 instrument at 23 °C, with 15-30 μM Bcl-xL in the ITC cell and 200-350 μM Bid_{BH3} peptide in the injection syringe, in NMR buffer. Protein and peptide concentrations were estimated from absorbance at 280 nm. The data were analyzed using Microcal ORIGIN software. Dissociation constants (Kd) were derived by fitting the data to a single-site binding model. Control titrations were performed by titrating peptide into either buffer or empty nanodiscs in buffer without Bcl-xL (Fig. S3).

RESULTS AND DISCUSSION

***Conformation of soluble Bcl-xL*.** We expressed and purified wild-type, full-length Bcl-xL using an intein-based *E. coli* expression system (39) that drives target protein production as an N-terminal fusion. Previously, we showed that expression systems with the reverse configuration, where Bcl-xL is the C-terminal fusion partner, result in truncation after M218 (36). The intein system, by contrast, yields intact, soluble Bcl-xL as confirmed by SDS-PAGE and mass spectrometry (Fig. S1C, D). The protein solubility is low (~10%) and Bcl-xL accumulates predominantly (90%) in the insoluble cellular fraction. As noted previously, however, both the soluble or insoluble fractions of Bcl-xL can be purified and homogeneously refolded in lipid bilayer membranes (35, 36).

In the concentration range of ~60-100 μM, soluble Bcl-xL is predominantly monomeric (Fig. S1E) and yields well-resolved NMR spectra (Fig. 1A). This result is in line with the very high (~600 μM) dissociation constant for dimer formation that has been reported based on fluorescence quenching experiments (56). In cells and *in vitro*, soluble Bcl-xL has been proposed to form dimers in which the tail of one monomer associates with the BH3-binding grove of the other (56, 57). *In vitro*, however, the $^{1}H/^{15}N$ NMR spectra show no evidence of such dimerization.

The $^{1}H/^{15}N$ NMR spectrum of full-length Bcl-xL is similar to that of tail-truncated protein (Bcl-xL-ΔC), indicating that the tail does not disrupt the general three-dimensional fold. Limited protein solubility and relatively low NMR signal intensity precluded *de novo* resonance assignment and structure determination, but several signals could be assigned by direct spectral comparison with the spectrum of Bcl-xL-ΔC (Table S1). In both cases, the spectrum is dominated by signals from the α1-α2 loop at 25°C, while raising the temperature to 45°C caused most tail peaks to disappear, indicating the presence of amide hydrogen exchange with water and/or conformational dynamics in the μsec-msec time scale for this region of the protein.

The chemical shift differences between tail-truncated and full-length Bcl-xL (Fig. 1B) are localized to specific proteins sites - in α2, α3, the α4-α5 loop and the end of α7 - that coincide primarily with the BH3-binding groove. The NH signals from G94, G138 and F146 are sentinels of the interactions of short BH3 peptides with the groove (58), while W169 and sites near the start of α6 are sensitive to more extensive engagement of the groove with longer BH3 peptides (58). Moreover, while most tail-induced perturbations localize to the folded domain, some are also observed in the long α1-α2 loop, at the polar opposite end of the BH3-binding groove. Overall, the NMR data reflect a protein conformation in which the tail associates with the groove and the conformational rearrangements associated with the tail-groove interaction are relayed to the loop.

To gain molecular insights about this soluble state of Bcl-xL we generated a protein model based on the NMR data and the existing structural information, and we performed all-atom MD simulations in aqueous solution. The initial model (Fig. S2D) was templated from the structure of the Bcl-xL/Bak-BH3 complex (Fig. S1A) (12), which lacks both tail (residues 210-233) and loop (residues 45-84) but has a BH3-bound head conformation, while the random conformation of the loop was taken from the structure of tail-truncated Bcl-xL (Fig. S1B) (11). The tail was taken from the NMR structure of the isolated C-terminal peptide (36, 37) and positioned in the groove by sequence-based alignment with the BH3 peptide in the Bcl-xL-Bak complex (12), noting that the Bcl-xL tail is restrained to bind the groove in the opposite sense to BH3 peptides, in a manner analogous to Bax (39). Five independent simulations were initiated from this model. After 1-μs MD simulation (Fig. 1C) the helical tail is associated with the surface groove, and helices α3 (residues 108-111) and α8 (residues 198-205) have unraveled to accommodate the tail. Notably, the loop undergoes a dramatic condensation from its initial extended structure, and packs loosely against α1 in the final conformation (Fig. 1C, Fig. S2D).

Within the limitations that our starting model for MD is not an experimentally determined structure of full-length Bcl-xL, and that our MD trajectories span a limited time scale of 1 μs, the resulting conformation is consistent with the NMR data and provides molecular insights about the cytosolic state of Bcl-xL. Viewed in the context of the MD simulation models, the $^{1}H/^{15}N$ chemical shift differences between tail-truncated and full-length Bcl-xL map predominantly to the BH3-binding groove, covering its entire topological length from G196 at one end to T115 at the other (Fig. 1C). The perturbation profile is reminiscent of, yet distinct from, the well-known high-affinity association of the groove with short BH3 peptides (58), which bind in the opposite sense with their N-terminus near the start of α4 (Fig. S2A). The large tail-induced chemical shift perturbations observed near residues 198-205 parallel the unraveling of α8 produced in the MD simulation. The NMR and MD data combined, demonstrate that the effects of the tail-groove interaction propagate allosterically from the groove, at one end of the Bcl-xL molecule, to α1 and the loop at the polar opposite end: association of the tail with the α3-α4 turn (T115) is sensed by α5-α6 sites (L162, E158, W169) one level below, and relayed to loop sites (F27, S28) two levels below (Fig. 1C, Fig. S3). As noted for Bcl-xL-ΔC (34), the data indicate that the loop, while disordered, is not totally conformationally disconnected from the head.

Membrane-anchored Bcl-xL. To examine the effects of the loop and tail on the membrane-anchored state of Bcl-xL, we reconstituted full-length protein in lipid bilayer nanodiscs, prepared with a 4/1 molar mixture of DMPC/DMPG, and the short membrane scaffold protein MSP1D1Δh5 (38). Size exclusion chromatography demonstrates that these Bcl-xL nanodiscs are homogeneously sized and have an apparent diameter similar to empty nanodiscs (Fig. S1E). The resulting $^{1}H/^{15}N$ NMR spectrum is very similar to that of loop-deleted Bcl-xL (Fig. 2A), indicating that the native full-length protein adopts a similar membrane-anchored conformation, with its C-terminal tail inserted across the nanodisc membrane. The data also demonstrate that reconstitution of the native protein sequence in lipid bilayers results in homogeneously folded preparations suitable for structural studies, without the need for non-native modifications of the sequence (37).

Notwithstanding the similarities between the NMR spectra of Bcl-xL and Bcl-xL-ΔL in nanodiscs, many differences are also apparent (Fig. 2B). Marked perturbations map to the loop excision sites in Bcl-xL-ΔL (residues E44 and A85), as expected, but prominent changes are also observed at more distal sites, specifically, residues 23-28 at the start of the loop, as well as α1, α2, α3, α7 and α8. The effect of the loop on the head is similar to that reported for soluble tail-truncated protein where the loop was shown to cause a subtle repositioning of α3 (34). The NMR data indicate that similar head-loop contacts are present in the membrane-anchored state of Bcl-xL.

Comparison with the NMR spectrum of soluble Bcl-xL-ΔC reveals the effects of membrane anchoring on the protein conformation (Fig. 2C). In this case, the chemical shift differences (Fig. 2D) map to the BH3-binding groove as well as the linker connecting α7 to the helical transmembrane tail. Interestingly, some perturbations are also observed in the loop, suggesting that the membrane lipids interact with both the globular head and loop of Bcl-xL.

To gain molecular insights about the membrane-anchored state, we performed all-atom MD simulations

of the protein in a lipid bilayer membrane with similar 4/1 molar composition of DMPC/DMPG as the experimental nanodiscs. The starting structural model was generated by appending the NMR structure of the membrane-inserted tail (36, 37) to tail-truncated Bcl-xL (11), and positioning it across the lipid bilayer (Fig. S2E, F). Five independent simulations were initiated from this model, each with different initial positions of the membrane lipids and different depth of tail insertion across the membrane. After 1-μs MD simulation, all five replicas remain membrane-embedded, and the protein adopts a preferred orientation in the membrane (Fig. 2E, F). The tail helix spans residues 207-230 and adopts a marked tilt of ~36° relative to the membrane normal (Fig. S4). Notably, the head also adopts a preferred average orientation that places the BH3-binding groove near the membrane surface while keeping it accessible to the aqueous milieu.

***Protein dynamics*.** NMR peak intensities provide a measure of a protein's propensity for chemical exchange and/or conformational flexibility in the μs-ms time scale. The soluble and membrane-anchored states of Bcl-xL exhibit generally similar $^{1}H/^{15}N$ peak intensity profiles (Fig. 3A). In both cases, the highest intensity sites coincide with the loop, in line with the absence of both electron density in the crystal structure and medium- to long-range NOEs in the NMR spectra for this region of the tail-truncated protein (11). In the case of soluble Bcl-xL, higher intensity is also apparent for the α3-α4 and α7-α8 regions, in line with helix unfolding at α3 (residues 108-111) and α8 (residues 199-205) to accommodate binding of the tail into the BH3 groove. For membrane-anchored Bcl-xL, higher intensity at residues 199-205 reflects the formation of a flexible linker that enables the head to reorient freely relative to the nanodisc membrane and allows the solution NMR spectrum to be detected. In both states, the intensity profile peaks at E39, S62 and R78, and exhibits distinct reduction around A50 and V65. The first half of the loop contains multiple negatively charged Glu and Asp residues whose mutually repulsive interactions may contribute to disorder and flexibility.

The intensity profile is more extremely defined for the membrane-anchored state. When each plot is internally normalized relative to the signal intensity from G24, a well resolved signal that can be measured with high accuracy, the maximum intensity of the membrane state is 10 times greater than that of the soluble state. We attribute this effect to the substantially slower overall tumbling rate of the nanodisc assembly (35), which causes general broadening and intensity reduction of NMR signals from the tail and head domains. It is, nevertheless, also possible that increased loop flexibility and/or hydrogen exchange rates are present in membrane-anchored Bcl-xL and contribute to this effect.

The MD simulations provide useful insight in this regard. The time-averaged root mean-square fluctuations (RMSF) calculated for heavy atoms over the last 500 ns of MD trajectories (Fig. 3B) parallel the experimental intensity profiles for all five replicas. The similarities with the NMR data are remarkable. As observed experimentally, both states have reduced fluctuations in the middle of the loop but the loop in the membrane-anchored state is twice as flexible as the soluble state. Importantly, this dynamic profile is observed across all five replicas of each state. Consistent with this observation, the conformation of the loop is compacted around α1 in solution and somewhat more expanded in the membrane. For membrane-anchored Bcl-xL, the very high RMSF of residues 199-233 parallels the unraveling of α8, and the motional decoupling of head and tail dynamics on the nanosecond time scale that is observed experimentally by NMR (35)

The profile of intramolecular contact frequencies (Fig. 3C), also calculated for heavy atoms over the last 500 ns of MD trajectories, further reveals that residues in the middle of the loop make frequent contact with other protein sites in the folded head domain, providing an explanation for their reduced flexibility compared to the rest of the loop in both soluble and membrane-anchored protein states. This is in line with the observation of ^{1}H-^{1}H NOE cross-peaks between the folded head and the W57 side chain in a deamidation mimicking loop mutant of soluble tail-truncated Bcl-xL (34). In the membrane-anchored state, this region of the loop also has some, albeit infrequent, encounters with the membrane surface (Fig. 3C), suggesting that fluctuations between contacts with the membrane and contacts with protein sites could contribute to enhanced loop dynamics. The contact map of membrane-anchored-Bcl-xL further reflects substantial contacts between sites in the BH3-binding groove – particularly α2-α4 – and the membrane lipids, including both the polar headgroups and hydrophobic acyl chains. This is in line

with the experimental membrane-induced chemical shift perturbations (Fig. 2D) and the preferred orientation of the head domain at the membrane surface (Fig. 2F). This feature is observed for all five independent trajectories (Fig. S5), although the frequency of membrane interaction with the head diminishes progressively for trajectories that were initiated after 1 Å increment translation from the membrane.

The loop and tail modulate the ligand binding activity of Bcl-xL. To examine the effects of the loop and tail on the BH3 binding characteristics of Bcl-xL, we performed ITC experiments with a peptide spanning residues 80-99 of the Bid BH3 motif (Bid_{BH3}). All binding isotherms reflect the 1:1 binding stoichiometry documented for the association of BH3 ligands with cytoprotective Bcl-2 proteins. Nevertheless, the binding affinity (Fig. 4A) of soluble full-length Bcl-xL for Bid_{BH3} is reduced by a factor of ~25 relative to either the isolated head domain (Bcl-xL-ΔLΔC) or the loop-head domains combined (Bcl-xL-ΔC). This is in line with the MD structural model of cytosolic Bcl-xL in which the tail associates with the BH3-binding groove, restricting access to other extramolecular ligands (Fig. 4C). The data reflect a BH3 binding event that involves competition with the protein's C-terminus.

In all three cases – Bcl-xL-ΔLΔC, Bcl-xL-ΔC, and Bcl-xL – the thermodynamic binding parameters (Fig. 4B) are dominated by favorable enthalpy (ΔH), consistent with the formation of residue-specific interactions between the groove and the BH3 ligand. However, while the BH3 binding interaction with Bcl-xL-ΔLΔC is purely enthalpy-driven and carries an unfavorable entropic factor associated with Bid_{BH3} helix formation from an unfolded state (58), BH3 binding to full-length Bcl-xL has a substantial favorable entropic component. The data indicate that displacement of the tail by the BH3 ligand likely contributes more than enough entropy gain to compensate for the entropy lost upon BH3 peptide folding. Interestingly, the loop contributes favorably to BH3 ligand affinity, enhancing the affinity of Bcl-xL-ΔC by a factor of ~1.6 relative to Bcl-xL-ΔLΔC. BH3 ligand binding in this case is accompanied by a favorable entropy increase (~2 kcal/mol).

A parallel effect is observed for the BH3-binding signature of membrane-anchored Bcl-xL (Fig. 4B). Here, the tail is membrane-inserted, leaving unrestricted access to the groove, and the loop contributes an additional positive entropic factor (~1.8 kcal/mol) to the binding free energy, enhancing the affinity by a factor of ~1.4 compared to Bcl-xL-ΔL. The MD simulations for this state show that even though the head is dynamically decoupled from the membrane-anchoring tail, it has a preferred orientation at the membrane surface (Fig. 4D). The BH3-binding groove is very close to the membrane surface but remains accessible to the aqueous milieu, consistent with the experimental ITC data showing high affinity of the membrane-anchored state for the BH3 peptide ligand.

These results reflect a coupling of the loop with the head in both the soluble and membrane-anchored states of Bcl-xL. The data indicate that the tail-groove interaction causes subtle conformational rearrangements that transmit allosterically to the distal loop, and that the loop must interact appreciably with the head to sense these perturbations.

CONCLUSIONS

Bcl-xL, like many of its Bcl-2 relatives that possess a membrane-anchoring tail, localizes predominantly to intracellular membranes. Endogenous Bcl-xL is integral to the mitochondrial outer membrane (59) and the C-terminal tail is essential for membrane integration and full functionality. Here we have shown that intact, wild-type Bcl-xL can be prepared for NMR structural studies of either the soluble or membrane-anchored states. Homogeneously folded preparations can be obtained in both cases without resorting to non-native protein truncations or modifications. This is important for advancing structural studies of Bcl-xL and other members of the Bcl-2 family, which have been limited primarily to tail-truncated protein constructs.

The NMR data obtained for Bcl-xL enable structural models of its soluble and membrane-anchored states to be generated for MD simulations, and the NMR and MD data combined provide new insights about the dynamics and ligand-binding activities of the protein in its native states. In solution, association of the tail with the globular head domain reduces the affinity of Bcl-xL for a Bid BH3 ligand

by a factor of ~25. A similar reduction in ligand affinity due to occlusion of the groove by the tail has been reported for Bcl-w (60, 61) and for forms of Bcl-xL encompassing part of the tail (35, 36, 62). Compared to these, the ~25-fold effect observed in this study is the most dramatic, indicating that the full inhibitory effect requires the complete length of the C-terminal tail of Bcl-xL. Contrary to studies where detergent micelles were used as membrane mimics, the Bcl-xL head domain adopts the same overall structure in both its soluble and membrane-anchored states, and retains similar BH3-binding properties. Moreover, in both states, the loop makes subtle contributions to the structure, dynamics and ligand-binding activity of Bcl-xL.

The globular head is thought to insert deeply into the membrane in response to physiological cues such as acidification (63, 64). Helices α1, α5 and α6 have been proposed to insert across the membrane based on NMR studies of Bcl-xL-ΔC in detergent micelles (65), and structural similarity to the pore-forming domains of bacterial toxins (11). Our previous solid-state NMR studies with Bcl-xL-ΔC reflected a shallow insertion of the head in the lipid bilayer (66). These early experiments were all performed in the absence of the C-terminus, and with sample conditions (low pH, detergent and ultrafiltration to concentrate the protein with liposomes) designed specifically to promote membrane-integration. It is possible that such a deeply membrane-embedded states reflect the late stages of apoptosis, where the program is committed to cell death and the mitochondrial membrane is permeabilized. The models presented in this study, by contrast more likely reflect the cytosolic and membrane-anchored states of Bcl-xL in the early stages of the apoptosis program or when the balance is shifted towards promoting cytoprotection. As the balance shifts toward cell death, the water-soluble head of Bcl-xL may become further integrated in the membrane.

Bcl-xL has also been reported to translocate between cytosolic and membrane-anchored states. How might this occur? The water solubility of wild-type, full-length Bcl-xL is highly curtailed, raising the question whether additional factors assist its shuttling between cellular compartments. Previously, we showed that truncated Bid, the caspase-8 cleavage product of Bid, is capable of associating with phospholipids to form nanometer size, lipoprotein particles, that are soluble and retain binding affinity for Bcl-xL (67). This points to a potential role of lipids in mediating Bcl-2 protein mobility and interactions. Lipid mobility is a hallmark of apoptosis (68-73) and lipid redistribution among cellular compartments is highly dynamic (74). Recent studies (75-77) suggest that lipid-assisted cytoplasmic mobility is important for shuttling Bcl-2 proteins to and from the mitochondrial outer membrane. Rather than adopting exclusively lipid-free or membrane-anchored states, Bcl-xL and its Bcl-2 relatives may lead less binary lifestyles, with lipids as key partners.

SUPPORTING MATERIAL

Supporting Material can be found online.

AUTHOR CONTRIBUTIONS

PR, YT, YY, AAB performed experiments.

PR, YT, YY, WI, and FMM analyzed data.

FMM and PR wrote the manuscript.

FMM designed the study

ACKNOWLEDGEMENTS

We thank Guy Salvesen for discussion. This study was supported by grants from the National Institutes of Health (CA 179087 and GM 118186 to FMM) and the National Science Foundation (MCB-1727508, MCB-1810695 and XSEDE MCB-070009 to WI). It utilized the Structural Biology Resource supported

by grant P30 CA030199.

REFERENCES

1. Boise, L. H., M. Gonzalez-Garcia, C. E. Postema, L. Ding, T. Lindsten, L. A. Turka, X. Mao, G. Nunez, and C. B. Thompson. 1993. bcl-x, a bcl-2-related gene that functions as a dominant regulator of apoptotic cell death. Cell 74(4):597-608.

2. Kvansakul, M., and M. G. Hinds. 2013. Structural biology of the Bcl-2 family and its mimicry by viral proteins. Cell death & disease 4:e909.

3. Lee, E. F., and W. D. Fairlie. 2019. The Structural Biology of Bcl-xL. Int J Mol Sci 20(9).

4. Gonzalez-Garcia, M., R. Perez-Ballestero, L. Ding, L. Duan, L. H. Boise, C. B. Thompson, and G. Nunez. 1994. bcl-XL is the major bcl-x mRNA form expressed during murine development and its product localizes to mitochondria. Development 120(10):3033-3042.

5. Fang, W., J. J. Rivard, D. L. Mueller, and T. W. Behrens. 1994. Cloning and molecular characterization of mouse bcl-x in B and T lymphocytes. Journal of immunology 153(10):4388-4398.

6. Mizuguchi, M., O. Sohma, S. Takashima, K. Ikeda, M. Yamada, N. Shiraiwa, and S. Ohta. 1996. Immunochemical and immunohistochemical localization of Bcl-x protein in the rat central nervous system. Brain research 712(2):281-286.

7. Hsu, Y. T., K. G. Wolter, and R. J. Youle. 1997. Cytosol-to-membrane redistribution of Bax and Bcl-X(L) during apoptosis. Proceedings of the National Academy of Sciences of the United States of America 94(8):3668-3672.

8. Edlich, F., S. Banerjee, M. Suzuki, M. M. Cleland, D. Arnoult, C. Wang, A. Neutzner, N. Tjandra, and R. J. Youle. 2011. Bcl-x(L) retrotranslocates Bax from the mitochondria into the cytosol. Cell 145(1):104-116.

9. Todt, F., Z. Cakir, F. Reichenbach, R. J. Youle, and F. Edlich. 2013. The C-terminal helix of Bcl-x(L) mediates Bax retrotranslocation from the mitochondria. Cell Death Differ 20(2):333-342.

10. Strasser, A., S. Cory, and J. M. Adams. 2011. Deciphering the rules of programmed cell death to improve therapy of cancer and other diseases. Embo J 30(18):3667-3683.

11. Muchmore, S. W., M. Sattler, H. Liang, R. P. Meadows, J. E. Harlan, H. S. Yoon, D. Nettesheim, B. S. Chang, C. B. Thompson, S. L. Wong, S. L. Ng, and S. W. Fesik. 1996. X-ray and NMR structure of human Bcl-xL, an inhibitor of programmed cell death. Nature 381(6580):335-341.

12. Sattler, M., H. Liang, D. Nettesheim, R. P. Meadows, J. E. Harlan, M. Eberstadt, H. S. Yoon, S. B. Shuker, B. S. Chang, A. J. Minn, C. B. Thompson, and S. W. Fesik. 1997. Structure of Bcl-xL-Bak peptide complex: recognition between regulators of apoptosis. Science 275(5302):983-986.

13. Maundrell, K., B. Antonsson, E. Magnenat, M. Camps, M. Muda, C. Chabert, C. Gillieron, U. Boschert, E. VialKnecht, J. C. Martinou, and S. Arkinstall. 1997. Bcl-2 undergoes phosphorylation by c-Jun N-terminal kinase stress-activated protein kinases in the presence of the constitutively active GTP-binding protein Rac1. J Biol Chem 272(40):25238-25242.

14. Clem, R. J., E. H. Cheng, C. L. Karp, D. G. Kirsch, K. Ueno, A. Takahashi, M. B. Kastan, D. E. Griffin, W. C. Earnshaw, M. A. Veliuona, and J. M. Hardwick. 1998. Modulation of cell death by Bcl-XL through caspase interaction. Proc Natl Acad Sci U S A 95(2):554-559.

15. Fang, G. F., B. S. Chang, C. N. Kim, C. Perkins, C. B. Thompson, and K. N. Bhalla. 1998. "Loop" domain is necessary for taxol-induced mobility shift and phosphorylation of Bcl-2 as well as for inhibiting taxol-induced cytosolic Accumulation of cytochrome c and apoptosis. Cancer Res 58(15):3202-3208.

16. Fujita, N., A. Nagahashi, K. Nagashima, S. Rokudai, and T. Tsuruo. 1998. Acceleration of apoptotic cell death after the cleavage of Bcl-X-L protein by caspase-3-like proteases. Oncogene 17(10):1295-1304.

17. Kirsch, D. G., A. Doseff, B. N. Chau, D. S. Lim, N. C. de Souza-Pinto, R. Hansford, M. B. Kastan, Y. A. Lazebnik, and J. M. Hardwick. 1999. Caspase-3-dependent cleavage of Bcl-2 promotes release of cytochrome c. J Biol Chem 274(30):21155-21161.

18. Srivastava, R. K., Q. S. Mi, J. M. Hardwick, and D. L. Longo. 1999. Deletion of the loop region of Bcl-2 completely blocks paclitaxel-induced apoptosis. Proc Natl Acad Sci U S A 96(7):3775-3780.

19. Yamamoto, K., H. Ichijo, and S. J. Korsmeyer. 1999. BCL-2 is phosphorylated and inactivated by an ASK1/Jun N-terminal protein kinase pathway normally activated at G(2)/M. Mol Cell Biol 19(12):8469-8478.

20. Kharbanda, S., S. Saxena, K. Yoshida, P. Pandey, M. Kaneki, Q. H. Wang, K. D. Cheng, Y. N. Chen, A. Campbell, T. Sudha, Z. M. Yuan, J. Narula, R. Weichselbaum, C. Nalin, and D. Kufe. 2000. Translocation of SAPK/JNK to mitochondria and interaction with Bcl-x(L) in response to DNA damage (vol 275, pg 322, 2000). J Biol Chem 275(25):19433-19433.

21. Basu, A., and S. Haldar. 2003. Identification of a novel Bcl-xL phosphorylation site regulating the sensitivity of taxol- or 2-methoxyestradiol-induced apoptosis. Febs Lett 538(1-3):41-47.

22. Du, L. H., C. S. Lyle, and T. C. Chambers. 2005. Characterization of vinblastine-induced Bcl-xL and Bcl-2 phosphorylation: evidence for a novel protein kinase and a coordinated phosphorylation/dephosphorylation cycle associated with apoptosis induction. Oncogene 24(1):107-117.

23. Schmitt, E., M. Beauchemin, and R. Bertrand. 2007. Nuclear colocalization and interaction between bcl-xL and cdk1(cdc2) duringG(2)/M cell-cycle checkpoint. Oncogene 26(40):5851-5865.

24. Zhao, R., D. Oxley, T. S. Smith, G. A. Follows, A. R. Green, and D. R. Alexander. 2007. DNA damage-induced Bcl-x(L) deamidation is mediated by NHE-1 antiport regulated intracellular pH. Plos Biol 5(1):39-53.

25. Asakura, T., K. Maeda, H. Omi, H. Matsudaira, and K. Ohkawa. 2008. The association of deamidation of Bcl-xL and translocation of Bax to the mitochondria through activation of JNK in the induction of apoptosis by treatment with GSH-conjugated DXR. Int J Oncol 33(2):389-395.

26. Upreti, M., E. N. Galitovskaya, R. Chu, A. J. Tackett, D. T. Terrano, S. Granell, and T. C. Chambers. 2008. Identification of the Major Phosphorylation Site in Bcl-xL Induced by Microtubule Inhibitors and Analysis of Its Functional Significance. J Biol Chem 283(51):35517-35525.

27. Wei, Y. J., S. Sinha, and B. Levine. 2008. Dual role of JNK1-mediated phosphorylation of Bcl-2 in autophagy and apoptosis regulation. Autophagy 4(7):949-951.

28. Tamura, Y., S. Simizu, M. Muroi, S. Takagi, M. Kawatani, N. Watanabe, and H. Osada. 2009. Polo-like kinase 1 phosphorylates and regulates Bcl-x(L) during pironetin-induced apoptosis. Oncogene 28(1):107-116.

29. Terrano, D. T., M. Upreti, and T. C. Chambers. 2010. Cyclin-Dependent Kinase 1-Mediated Bcl-x(L)/Bcl-2 Phosphorylation Acts as a Functional Link Coupling Mitotic Arrest and Apoptosis. Mol Cell Biol 30(3):640-656.

30. Dho, S. H., B. E. Deverman, C. Lapid, S. R. Manson, L. Gan, J. J. Riehm, R. Aurora, K. S. Kwon, and S. J. Weintraub. 2013. Control of Cellular Bcl-x(L) Levels by Deamidation-Regulated Degradation. Plos Biol 11(6).

31. Bah, N., L. Maillet, J. Ryan, S. Dubreil, F. Gautier, A. Letai, P. Juin, and S. Barille-Nion. 2014. Bcl-xL controls a switch between cell death modes during mitotic arrest (vol 5, e1291, 2014). Cell death & disease 5.

32. Kim, S. Y., X. X. Song, L. Zhang, D. L. Bartlett, and Y. J. Lee. 2014. Role of Bcl-xL/Beclin-1 in interplay between apoptosis and autophagy in oxaliplatin and bortezomib-induced cell death. Biochem Pharmacol 88(2):178-188.

33. Maiuri, M. C., G. Le Toumelin, A. Criollo, J. C. Rain, F. Gautier, P. Juin, E. Tasdemir, G. Pierron, K. Troulinaki, N. Tavernarakis, J. A. Hickman, O. Geneste, and G. Kroemer. 2007. Functional and physical interaction between Bcl-X-L and a BH3-like domain in Beclin-1. Embo J 26(10):2527-2539.

34. Follis, A. V., F. Llambi, H. Kalkavan, Y. Yao, A. H. Phillips, C. G. Park, F. M. Marassi, D. R. Green, and R. W. Kriwacki. 2018. Regulation of apoptosis by an intrinsically disordered region of Bcl-xL. Nat Chem Biol 14(5):458-465.

35. Yao, Y., L. M. Fujimoto, N. Hirshman, A. A. Bobkov, A. Antignani, R. J. Youle, and F. M. Marassi. 2015. Conformation of BCL-XL upon Membrane Integration. J Mol Biol 427(13):2262-2270.

36. Yao, Y., D. Nisan, L. M. Fujimoto, A. Antignani, A. Barnes, N. Tjandra, R. J. Youle, and F. M. Marassi. 2016. Characterization of the membrane-inserted C-terminus of cytoprotective BCL-XL. Protein Expr Purif 122:56-63.

37. Raltchev, K., J. Pipercevic, and F. Hagn. 2018. Production and Structural Analysis of Membrane-Anchored Proteins in Phospholipid Nanodiscs. Chemistry 24(21):5493-5499.

38. Hagn, F., M. Etzkorn, T. Raschle, and G. Wagner. 2013. Optimized phospholipid bilayer nanodiscs facilitate high-resolution structure determination of membrane proteins. Journal of the American Chemical Society 135(5):1919-1925.

39. Suzuki, M., R. J. Youle, and N. Tjandra. 2000. Structure of Bax: coregulation of dimer formation and intracellular localization. Cell 103(4):645-654.

40. Cavanagh, J., W. J. Fairbrother, A. G. Palmer, and N. J. Skelton. 1996. Protein NMR spectroscopy : principles and practice. Academic Press, San Diego.

41. Grzesiek, S., and A. Bax. 1992. Improved 3D triple-resonance NMR techniques applied to a 31 kDa protein. Journal of Magnetic Resonance (1969) 96(2):432-440.

42. Wittekind, M., and L. Mueller. 1993. HNCACB, a High-Sensitivity 3D NMR Experiment to Correlate Amide-Proton and Nitrogen Resonances with the Alpha- and Beta-Carbon Resonances in Proteins. Journal of Magnetic Resonance, Series B 101(2):201-205.

43. Cornilescu, G., F. Delaglio, and A. Bax. 1999. Protein backbone angle restraints from searching a database for chemical shift and sequence homology. J Biomol NMR 13(3):289-302.

44. Shen, Y., F. Delaglio, G. Cornilescu, and A. Bax. 2009. TALOS+: a hybrid method for predicting protein backbone torsion angles from NMR chemical shifts. Journal of Biomolecular NMR 44(4):213-223.

45. Skinner, S. P., R. H. Fogh, W. Boucher, T. J. Ragan, L. G. Mureddu, and G. W. Vuister. 2016. CcpNmr AnalysisAssign: a flexible platform for integrated NMR analysis. J Biomol NMR 66(2):111-124.

46. Brooks, B. R., C. L. Brooks, 3rd, A. D. Mackerell, Jr., L. Nilsson, R. J. Petrella, B. Roux, Y. Won, G. Archontis, C. Bartels, S. Boresch, A. Caflisch, L. Caves, Q. Cui, A. R. Dinner, M. Feig, S. Fischer, J. Gao, M. Hodoscek, W. Im, K. Kuczera, T. Lazaridis, J. Ma, V. Ovchinnikov, E. Paci, R. W. Pastor, C. B. Post, J. Z. Pu, M. Schaefer, B. Tidor, R. M. Venable, H. L. Woodcock, X. Wu, W. Yang, D. M. York, and M. Karplus. 2009. CHARMM: the biomolecular simulation program. J Comput Chem 30(10):1545-1614.

47. Hatcher, E., O. Guvench, and A. D. Mackerell. 2009. CHARMM additive all-atom force field for aldopentofuranoses, methyl-aldopentofuranosides, and fructofuranose. J Phys Chem B 113(37):12466-12476.

48. Klauda, J. B., R. M. Venable, J. A. Freites, J. W. O'Connor, D. J. Tobias, C. Mondragon-Ramirez, I. Vorobyov, A. D. MacKerell, Jr., and R. W. Pastor. 2010. Update of the CHARMM all-atom additive force field for lipids: validation on six lipid types. J Phys Chem B 114(23):7830-7843.

49. Jorgensen, W. L., J. Chandrasekhar, J. D. Madura, R. W. Impey, and M. L. Klein. 1983. Comparison of simple potential functions for simulating liquid water. The Journal of Chemical Physics 79(2):926-935.

50. Singh, C., H. Lee, Y. Tian, S. S. Bartra, S. Hower, L. M. Fujimoto, Y. Yao, S. A. Ivanov, R. Z. Shaikhutdinova, A. P. Anisimov, G. V. Plano, W. Im, and F. M. Marassi. 2020. Mutually constructive roles of Ail and LPS in Yersinia pestis serum survival. Mol. Microbiol.

51. Jo, S., T. Kim, V. G. Iyer, and W. Im. 2008. CHARMM-GUI: a web-based graphical user interface for CHARMM. J. Comput. Chem. 29(11):1859-1865.

52. Jo, S., J. B. Lim, J. B. Klauda, and W. Im. 2009. CHARMM-GUI Membrane Builder for mixed bilayers and its application to yeast membranes. Biophys. J. 97(1):50-58.

53. Wu, E. L., X. Cheng, S. Jo, H. Rui, K. C. Song, E. M. Davila-Contreras, Y. Qi, J. Lee, V. Monje-Galvan, R. M. Venable, J. B. Klauda, and W. Im. 2014. CHARMM-GUI Membrane Builder toward realistic biological membrane simulations. J. Comput. Chem. 35(27):1997-2004.

54. Lee, J., D. S. Patel, J. Stahle, S. J. Park, N. R. Kern, S. Kim, J. Lee, X. Cheng, M. A. Valvano, O. Holst, Y. A. Knirel, Y. Qi, S. Jo, J. B. Klauda, G. Widmalm, and W. Im. 2019. CHARMM-GUI Membrane Builder for Complex Biological Membrane Simulations with Glycolipids and Lipoglycans. Journal of chemical theory and computation 15(1):775-786.

55. Eastman, P., M. S. Friedrichs, J. D. Chodera, R. J. Radmer, C. M. Bruns, J. P. Ku, K. A. Beauchamp, T. J. Lane, L. P. Wang, D. Shukla, T. Tye, M. Houston, T. Stich, C. Klein, M. R. Shirts, and V. S. Pande. 2013. OpenMM 4: A Reusable, Extensible, Hardware Independent Library for High Performance Molecular Simulation. J Chem Theory Comput 9(1):461-469.

551 56. Bleicken, S., A. Hantusch, K. K. Das, T. Frickey, and A. J. Garcia-Saez. 2017. Quantitative
552 interactome of a membrane Bcl-2 network identifies a hierarchy of complexes for apoptosis
553 regulation. Nat Commun 8(1):73.

554 57. Jeong, S. Y., B. Gaume, Y. J. Lee, Y. T. Hsu, S. W. Ryu, S. H. Yoon, and R. J. Youle. 2004. Bcl-x(L)
555 sequesters its C-terminal membrane anchor in soluble, cytosolic homodimers. EMBO Journal
556 23(10):2146-2155.

557 58. Yao, Y., A. A. Bobkov, L. A. Plesniak, and F. M. Marassi. 2009. Mapping the interaction of pro-
558 apoptotic tBID with pro-survival BCL-XL. Biochemistry 48(36):8704-8711.

559 59. Kaufmann, T., S. Schlipf, J. Sanz, K. Neubert, R. Stein, and C. Borner. 2003. Characterization of the
560 signal that directs Bcl-x(L), but not Bcl-2, to the mitochondrial outer membrane. J. Cell Biol.
561 160(1):53-64.

562 60. Denisov, A. Y., M. S. Madiraju, G. Chen, A. Khadir, P. Beauparlant, G. Attardo, G. C. Shore, and K.
563 Gehring. 2003. Solution structure of human BCL-w: modulation of ligand binding by the C-terminal
564 helix. J Biol Chem 278(23):21124-21128.

565 61. Hinds, M. G., M. Lackmann, G. L. Skea, P. J. Harrison, D. C. Huang, and C. L. Day. 2003. The
566 structure of Bcl-w reveals a role for the C-terminal residues in modulating biological activity. Embo J
567 22(7):1497-1507.

568 62. Walensky, L. D., K. Pitter, J. Morash, K. J. Oh, S. Barbuto, J. Fisher, E. Smith, G. L. Verdine, and S.
569 J. Korsmeyer. 2006. A stapled BID BH3 helix directly binds and activates BAX. Molecular Cell
570 24(2):199-210.

571 63. Minn, A. J., P. Velez, S. L. Schendel, H. Liang, S. W. Muchmore, S. W. Fesik, M. Fill, and C. B.
572 Thompson. 1997. Bcl-x(L) forms an ion channel in synthetic lipid membranes. Nature 385(6614):353-
573 357.

574 64. Thuduppathy, G. R., J. W. Craig, V. Kholodenko, A. Schon, and R. B. Hill. 2006. Evidence that
575 membrane insertion of the cytosolic domain of Bcl-xL is governed by an electrostatic mechanism. J.
576 Mol. Biol. 359(4):1045-1058.

577 65. Losonczi, J. A., E. T. Olejniczak, S. F. Betz, J. E. Harlan, J. Mack, and S. W. Fesik. 2000. NMR
578 studies of the anti-apoptotic protein Bcl-xL in micelles. Biochemistry 39(36):11024-11033.

579 66. Franzin, C. M., J. Choi, D. Zhai, J. C. Reed, and F. M. Marassi. 2004. Structural studies of apoptosis
580 and ion transport regulatory proteins in membranes. Magn. Reson. Chem. 42(2):172-179.

581 67. Ekanayake, V., D. Nisan, P. Ryzhov, Y. Yao, and F. M. Marassi. 2018. Lipoprotein Particle Formation
582 by Proapoptotic tBid. Biophys. J. 115(3):533-542.

583 68. Hakumaki, J. M., H. Poptani, A. M. Sandmair, S. Yla-Herttuala, and R. A. Kauppinen. 1999. 1H MRS
584 detects polyunsaturated fatty acid accumulation during gene therapy of glioma: implications for the
585 in vivo detection of apoptosis. Nat. Med. 5(11):1323-1327.

586 69. Delikatny, E. J., W. A. Cooper, S. Brammah, N. Sathasivam, and D. C. Rideout. 2002. Nuclear
587 magnetic resonance-visible lipids induced by cationic lipophilic chemotherapeutic agents are
588 accompanied by increased lipid droplet formation and damaged mitochondria. Cancer Res.
589 62(5):1394-1400.

590 70. Iorio, E., M. Di Vito, F. Spadaro, C. Ramoni, E. Lococo, R. Carnevale, L. Lenti, R. Strom, and F.
591 Podo. 2003. Triacsin C inhibits the formation of 1H NMR-visible mobile lipids and lipid bodies in HuT
592 78 apoptotic cells. Biochim Biophys Acta 1634(1-2):1-14.

593 71. Blankenberg, F. G. 2008. In vivo detection of apoptosis. J. Nucl. Med. 49 Suppl 2:81S-95S.

594 72. Quintero, M., M. E. Cabanas, and C. Arus. 2010. 13C-labelling studies indicate compartmentalized
595 synthesis of triacylglycerols in C6 rat glioma cells. Biochim Biophys Acta 1801(7):693-701.

596 73. Boren, J., and K. M. Brindle. 2012. Apoptosis-induced mitochondrial dysfunction causes cytoplasmic
597 lipid droplet formation. Cell Death Differ 19(9):1561-1570.

598 74. Degli Esposti, M., P. Matarrese, A. Tinari, A. Longo, S. Recalchi, R. Khosravi-Far, W. Malorni, R.
599 Misasi, T. Garofalo, and M. Sorice. 2017. Changes in membrane lipids drive increased endocytosis
600 following Fas ligation. Apoptosis 22(5):681-695.

601 75. Chen, R., A. E. Feldstein, and T. M. McIntyre. 2009. Suppression of mitochondrial function by
602 oxidatively truncated phospholipids is reversible, aided by bid, and suppressed by Bcl-XL. J. Biol.
603 Chem. 284(39):26297-26308.

604 76. Crimi, M., and M. D. Esposti. 2011. Apoptosis-induced changes in mitochondrial lipids. Biochim
605 Biophys Acta 1813(4):551-557.

606 77. Bischof, J., M. Salzmann, M. K. Streubel, J. Hasek, F. Geltinger, J. Duschl, N. Bresgen, P. Briza, D.
607 Haskova, R. Lejskova, M. Sopjani, K. Richter, and M. Rinnerthaler. 2017. Clearing the outer
608 mitochondrial membrane from harmful proteins via lipid droplets. Cell Death Discov 3:17016.
609

610

611

FIGURE LEGENDS

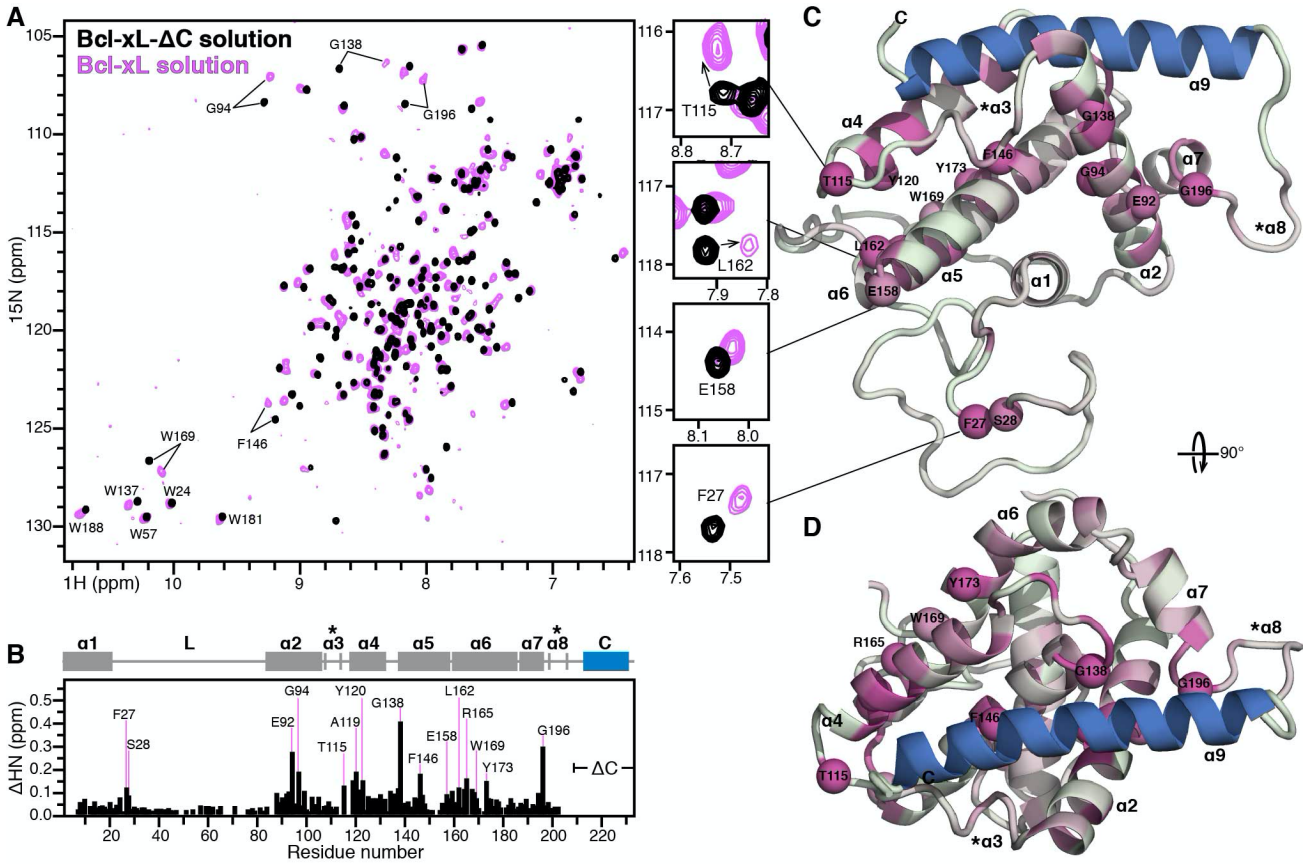

Figure 1. Conformation of soluble full-length Bcl-xL. (A) ^{1}H/^{15}N HSQC NMR spectra of ^{15}N labeled Bcl-xL-ΔC (black) and wild-type Bcl-xL (mauve). The spectra were recorded at 45°C. Selected regions are expanded to highlight specific perturbation sites. **(B)** Profile of tail-induced chemical shift perturbations across the sequence of Bcl-xL. Bars represent the combined difference (ΔHN) of amide ^{1}H and ^{15}N chemical shifts. Helix boundaries are taken from the original structures of Bcl-xL (11, 12). **(C, D)** Orthogonal views of the structural model of soluble Bcl-xL taken after 1-μs MD simulation. Colors reflect the magnitude of ΔHN from 0 ppm (gray) to the maximum value (0.39 ppm, pink). N atoms of highly perturbed sites are shown as spheres. The tail is colored blue. Asterisks denote unraveling in helices α3 and α8. The loop is not shown in panel D.

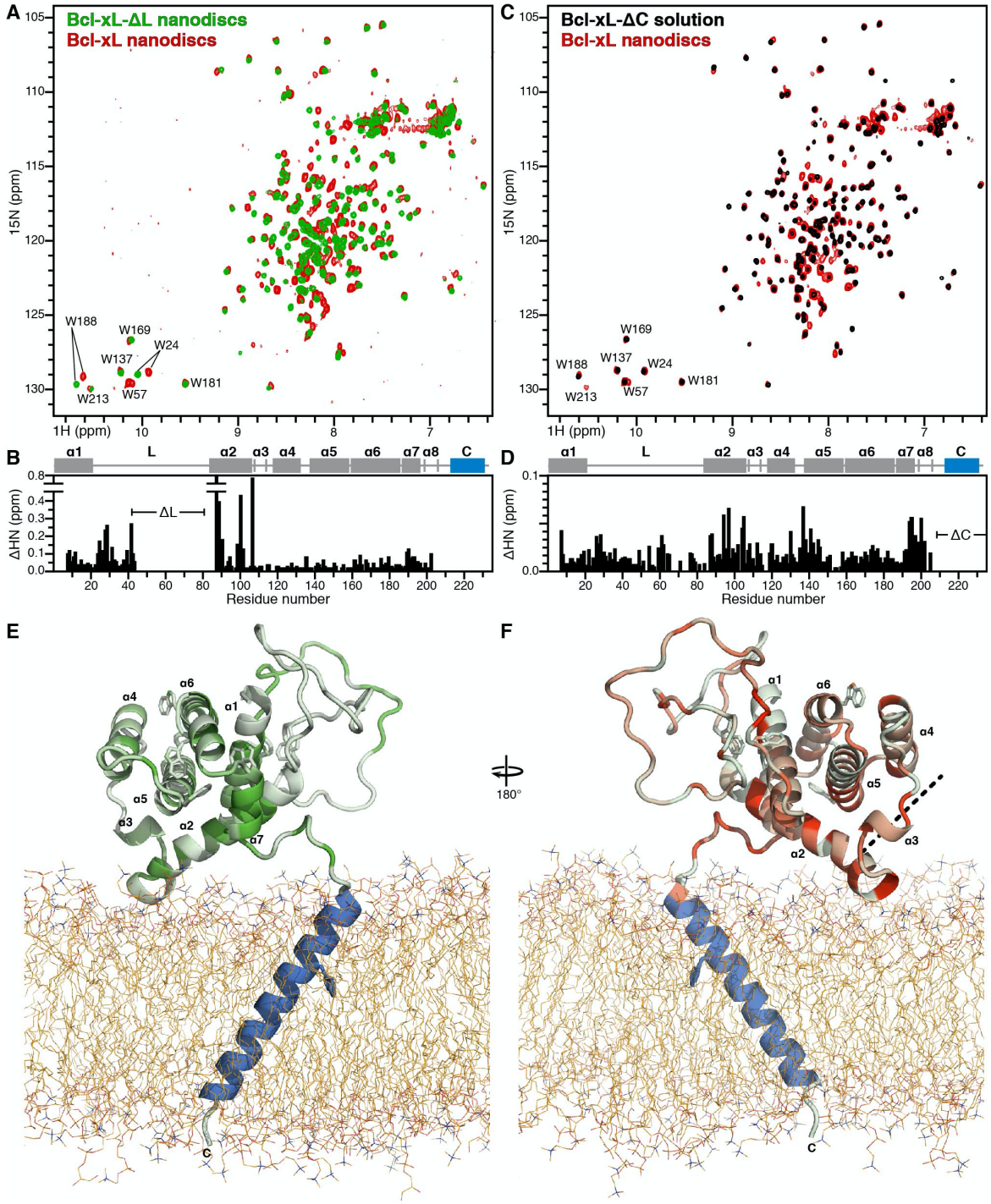

Figure 2. Effects of membrane-anchoring on the head and loop of Bcl-xL. (A, C) $^{1}H/^{15}N$ HSQC NMR spectra of ^{15}N labeled wild-type Bcl-xL (red) in nanodiscs, Bcl-xL-ΔL in nanodiscs (green) and Bcl-xL-ΔC in solution (black), recorded at 45°C. **(B, D)** Chemical shift perturbations across the sequence of Bcl-xL, induced by the loop in nanodiscs (B), or by membrane-inserted tail (D). Bars represent the combined difference (ΔHN) of amide ^{1}H and ^{15}N chemical shifts. Helix boundaries are taken from the model of membrane-inserted Bcl-xL after 1-μs MD. **(E, F)** 180° Views of membrane-anchored Bcl-xL taken after 1-μs MD simulation. Colors reflect the magnitude of ΔHN from 0 ppm (gray) to the maximum value in B (0.81 ppm, green) or D (0.07 ppm, red). The tail is colored blue. The dashed line marks the position of the BH3-binding groove.

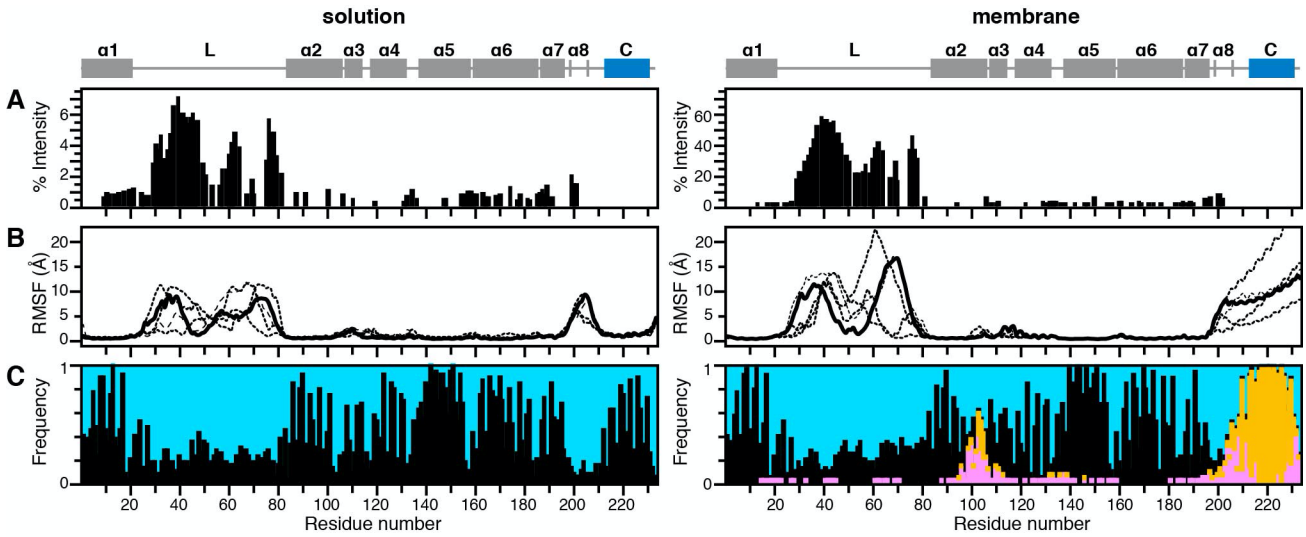

Figure 3. NMR Peak intensity, MD flexibility and MD interaction profiles of soluble (left) and membrane-anchored (right) Bcl-xL. (A) Percent $^{1}H/^{15}N$ HSQC peak intensities, normalized to the signal from G21 at 1%. **(B)** Time-averaged RMSF calculated for heavy atoms over the last 500 ns of 1-μs MD trajectories for five independent replicas. The profile for one replica is highlighted (solid line). Protein alignment was relative to the head (residues 1-22 and 82-196). **(C)** Interaction profile of protein residues with their environment. The bars represent frequency of occurrence within 4 Å of water (blue), phospholipid head groups (pink) or tails (gold), or protein sites (black). Each data point is the average over the last 500 ns of 1-μs MD trajectories and over five independent replicas.

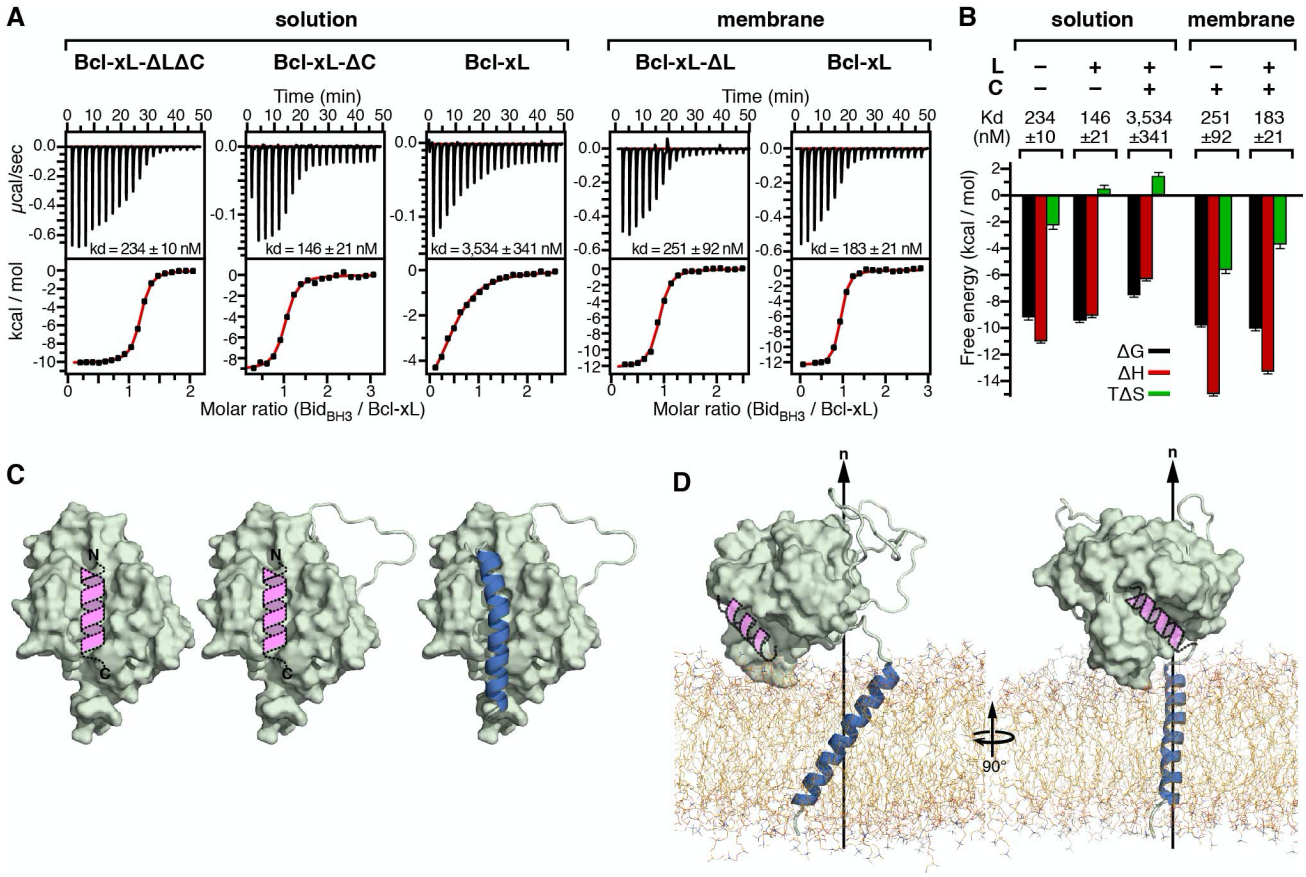

Figure 4. ITC titrations of Bid$_{BH3}$ peptide into Bcl-xL. (A) Representative calorimetric data (top) and integrated heat (bottom) are shown as a function of Bid$_{BH3}$/Bcl-xL molar ratio. The data were corrected for non-specific binding by subtracting control ITC titrations performed by titrating peptide into buffer or empty nanodiscs without Bcl-xL (Fig. S3). Solid lines (red) are the best fits of the binding isotherms to a single-site binding model, used to extract the values of the dissociation constant (K_d). **(B)** Plot of the thermodynamic parameters for each calorimetric titration. Values represent the average of triplicate or duplicate titrations and error bars represent standard deviation. **(C, D)** Representative snapshots (taken at 1 μs) of MD simulations of Bcl-xL in solution (C) or anchored to the membrane (D). The globular head is shown as a surface. In solution (C), the helical tail (blue) tucks into the BH3-binding groove blocking BH3 ligand binding. Deletion of the tail frees the groove and makes accessible to a BH3 ligand (pink). In the membrane (D), the tail spans the bilayer and head adopts a preferred average orientation relative to the membrane surface that allows the groove to engage with its BH3 ligands (pink).